Bridging molecular and nanoparticle scale kinetic regimes in the crystallization of icosahedral gold nanoparticles

Raj Kumar Ramamoorthy,[1,2,†] Rohan Parmar,[3,†] Ezgi Yildirim,[1] Marie Brut,[4] Sylvain David,[3] Simon Cayez,[1] Nicolas Ratel-Ramond,[1] Pierre Roblin,[3] Fabien Delpech,[1] Isaac Rodriguez-Ruiz,[3] Lise-Marie Lacroix,[1,5] Sébastien Teychené,[3,*] Guillaume Viau[1,*]

[1] Univ Toulouse, INSA, CNRS, LPCNO, Toulouse, France

[2] Nanoscale and Interface Science Laboratory, Department of Physics, Anna University, Chennai 600025, India

[3] Univ Toulouse, INP Toulouse, CNRS, LGC, Toulouse, France

[4] Univ Toulouse, CNRS, LAAS, Toulouse, France

[5] Institut Universitaire de France, IUF, Paris, France

Supplementary information

Table of contents

I. Experimental section

Chemicals

Hydrogen tetrachloroaurate trihydrate ($HAuCl_4 \cdot 3H_2O$, 99.99%, Alfa Aesar), triethylsilane (TES, 99%, Sigma-Aldrich), oleylamine (OY, 80-90%, Acros) and hexane (mixed isomer, 98+%, Alfa Aesar) were used as received.

Au(III) precursor suspensions

The Au(III) precursor solutions were prepared by dissolving $HAuCl_4.3H_2O$ in a solution of oleylamine (OY) in hexane. After sonication $HAuCl_4.3H_2O$ was completely dissolved and a pale-yellow solution was obtained. In the most of the reactions, the concentrations of Au^{III} and OY were fixed to 20 mM and 50 mM, respectively. When [Au^{III}] was decreased the molar ratio [Au^{III}]/[OY] was fixed to 2.5.

Au(0) nanoparticles synthesis

Solutions of TES in hexane were prepared at different TES concentration. The solutions were thermalized at the appropriate temperature with a water bath before mixing. After few minutes of thermalization, the TES solution was mixed to the Au precursor solution. The nominal concentrations of Au^{III} and OY in the mixture were fixed to 20 mM and 50 mM, respectively. When [Au^{III}] was decreased the molar ratio [Au^{III}]/[OY] was fixed to 2.5. The TES concentration was varied from 62 mM to 500 mM. After addition of TES, the color change from pale yellow to dark red-brown was almost instantaneous. The Au NPs suspensions were let to react three hours to insure a complete reduction yield.

TES oxidation products

To identify the silicon-based species present in the reaction medium, the gold NP solution at the end of the reaction was analyzed by ^{29}Si NMR (see experimental details below). The ^{29}Si NMR spectrum shows the residual presence of TES in excess (δ -0.2 ppm) and the formation of triethylchlorosilane (δ 34.0 ppm), as well as hexaethyldisiloxane (δ 8.6 ppm). These three compounds were identified by comparison with commercial pure standards. The formation of hexaethyldisiloxane most likely results from the hydrolysis of trichlorosilane, due to the presence of water molecules and catalyzed by H^+.

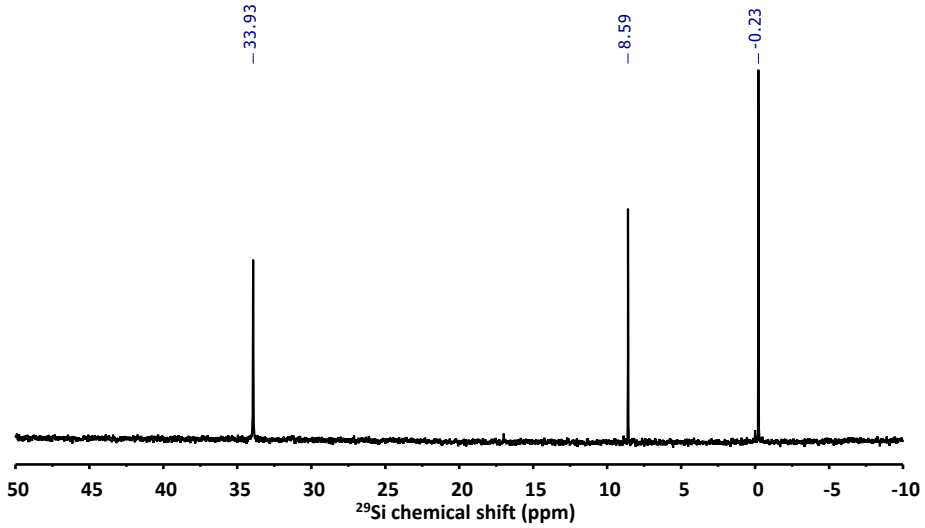

Figure S1. ^{29}Si NMR spectrum of Au NPs suspension prepared by reduction prepared by reduction of $HAuCl_4.3H_2O$ in OY/hexane with TES as reducing agent ([Au] = 20 mM; [OY]/[Au] = 2.5; [TES]= 62 mM). showing residual TES δ = - 0.2 ppm, triethylchlorosilane δ = 8.6 ppm and hexaethyldisiloxane δ = 34.0 ppm.

Considering that triethylchlorosilane is the main oxydation product corresponding to the reduction of gold chloride and that hexaethyldisiloxane as by-product of hydrolysis of trichlorosilane, the stoichiometry of the chemical reduction is given by :

$$HAuCl_4 + \frac{3}{2}R_3SiH + \frac{5}{2}C_{18}H_{35}NH_2 \rightarrow Au(0) + \frac{3}{2}R_3SiCl + \frac{5}{2}C_{18}H_{35}NH_3^+ Cl^-$$

1.5 equivalent of TES is required to fully convert Au^{III} in Au^0. TES was always added in large excess compared to the stoichiometry. The molar ratio [OY]/[Au] = 2.5 corresponds to the stoichiometry of the reaction, 1 eq. of OY being neutralized by the proton of $HAuCl_4$ and 1.5 eq. being neutralized by 1.5 eq. of H^+ released by the reaction of 1.5 eq. of TES. This was confirmed by the complete neutralization of oleylamine in oleylammonium chloride.

Density measurements

The density of the Au^{III} precursor suspensions were measured at room temperature with a density meter ANTON PAAR DMA 1001.

Small Angle X-ray Scattering (SAXS)

SAXS analysis of the Au(III) precursor and Au(0) NP suspensions were performed on a XEUSS 2.0 laboratory instrument equipped with a pixel detector PILATUS 1 M (DECTRIS) and a Cu Kα X-ray source provided by GeniX3D (λ = 1.54 Å). The sample to detector distance was fixed to record the SAXS signal in the q range 0.02-1 $Å^{-1}$. The fitting strategies depend on the system analyzed, they are described in the next sections.

High Energy X-ray Diffraction (HE-XRD) and Pair Distribution Function analysis

HE-XRD of the precursor and NP suspensions were collected at the ID15A beamline (ESRF, France) using a X-ray beam of energy 69 keV (λ = 0.1797Å) incident on a 1.5 mm diameter capillary containing either the precursor suspension or the nanoparticles in suspension in the mother liquor. The X-ray scattering patterns were recorded using a Pilatus 2M detector in the q-range from 0.2 to 22 $Å^{-1}$.

The pair distribution functions (PDFs) were extracted using the application PDFgetX3.[1] Nanoparticle structural models at the atomic scale were performed using an atomic simulation environment (ase) python library.[2] The experimental PDFs were then compared to theoretical PDFs of known similar structures. Least-square refinement of the experimental PDFs was done using the diffpy-cmi package.

Nuclear Magnetic Resonance

Solution NMR spectra were obtained on a Bruker Avance NEO 600 for ^1H NMR experiment and on a Bruker Avance III HD 500 MHz. ^1H NMR spectrum were recorded in cyclohexane-d12 at 293 K. Diffusion measurements (DOSY) were made using the stimulated echo pulse sequence. Chemical shifts were quoted relative to $SiMe_4$ (^1H and ^{29}Si).

Kinetic studies

Microfluidic set-up

Kinetic studies by X-ray absorption spectroscopy (XAS) and small angle X-ray scattering (SAXS) were performed in a homemade hybrid Kapton-OSTEMER (Mercene Labs, Sweden) microreactor already described in a previous study.[3] For completeness, a schematic of the cells and its operation is presented in figure S2. The cell comprises two inlets for reagent injection (circles A and B in Figure S2b) coupled to an ultra-fast microfluidic mixer with a butterfly-shape structure. Subsequently, the interrogation channel is conceived with a cross section of 2 x 2 mm. The cell can operate as a continuous flow reactor by continuously injecting the reagent solutions or as a stop-flow cell (Figure S2b) probing both short and long reaction times.

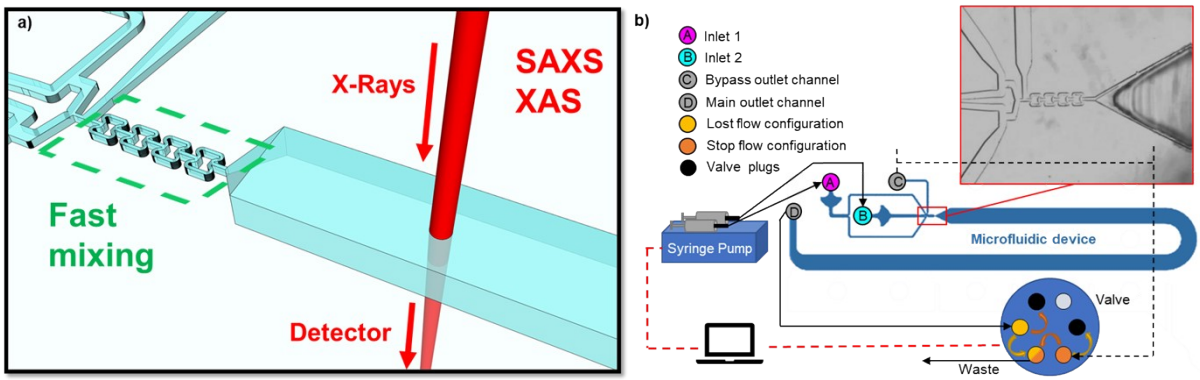

Figure S2. Schematic of the microreactor and experimental setup. The reactor comprises two inlets (A and B) for reagent injection using syringe pumps, a bypass channel (C) connected to a valve system that allows switching between continuous-flow and stop-flow modes, four butterfly mixers with a cross-section of 20 µm × 50 µm, a main observation channel for tracking the reaction progress, and a main outlet (D).

XAS experiments

The gold speciation was followed by XAS as a function of time. Time-resolved *in situ* XAS experiments were carried out at the SuperXAS beamline (PSI, Switzerland). XAS at the Au L_{III}-edge were recorded in fluorescence mode. Time-resolved XAS signals were collected in continuous flow for reaction times between 1 s and 30 s every 0.1 s and every 3 or 4 s in stopped flow for reaction times between 30 s and the end of the reaction. The time-resolved X-ray absorption near edge spectra (XANES) were analyzed by a linear combination analysis (LCA) of three spectra used as references for the Au(III), Au(I) and Au(0) oxidation states, which were respectively, the precursor solution obtained by dissolving $HAuCl_4$ in the solution of oleylamine in hexane, the OYAu(I)Cl lamellar phase and the final Au NPs. This method provided was described in details in previous studies.[4]

SAXS experiments

Time-resolved *in situ* small angle X-ray scattering (SAXS) experiments were carried out at the SWING beamline (Synchrotron SOLEIL, France). Experiments were conducted in transmission mode using an X-ray energy of 12 keV, and a beam size of 0.2 x 0.2 mm. A fixed sample-to-detector distance provided access to a scattering vector q-range of 10^{-2} – 1 $Å^{-1}$.

II. Analysis of the precursor suspensions – Characterization of the Au^{III} clusters

II.1 ^{1}H NMR

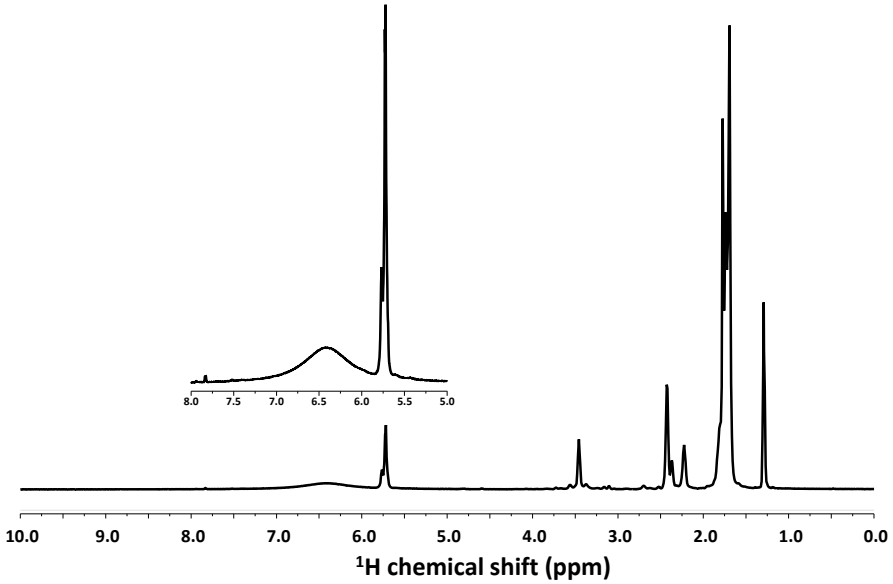

Figure S3. ^{1}H NMR spectrum of the precursor solution obtained by dissolution of $HAuCl_4.3H_2O$ in solution of oleylamine in cyclohexane-d12 ([Au] = 20 mM; [OY]/[Au] = 2.5).

II.2 SAXS Modelling

The *in situ* SAXS of the precursor solution obtained by dissolving $HAuCl_4.3H_2O$ in solution of oleylamine in hexane exhibit a strong signal (Fig. S4a). It shows that the dissolution of the gold precursor does not lead to homogeneous solution of free Au^{III} complexes but to the formation of nanostructured suspension containing clusters of Au^{III} complexes.

The SAXS of the precursor suspensions were analyzed with a Guinier-Porod model[5] using the software SasView 5.0.5.[6] The scattering intensity was fitted to Eq. S1:

$$I(q) = \frac{G}{Q^s} exp\left[\frac{-Q^2 R_g^2}{3-s}\right] \quad Q \leq Q_1$$
$$I(q) = D/Q^m \quad Q \geq Q_1 \qquad \text{(Eq. S1)}$$

where G and D are the Guinier and Porod scale factors, respectively, Q is the scattering variable where Q_1 is the point at which the derivatives of the Guinier and Porod terms are equal and continuous, m is the porod exponent, and R_g and s are the radius of gyration and dimensionality of the scattering objects, respectively.[7]

The diameter of the Au^{III} clusters was calculated according to :

$$D = 2 \times \sqrt{\frac{5}{3}} R_g \qquad \text{(Eq. S2)}$$

The fit results are summarized in Fig. S4b-d. In all cases, the best fits were obtained with *s* = 0 (spherical objects) and *m* = 4 (smooth interface). The diameter of the Au^{III} clusters was found to increase slightly from 3.6 to 4.2 nm when the Au concentration was increased from 1 to 20 mM (Fig. S4b). The scale factor, G, and the background values were found to increase linearly with the nominal concentration (Fig. S4c,d).

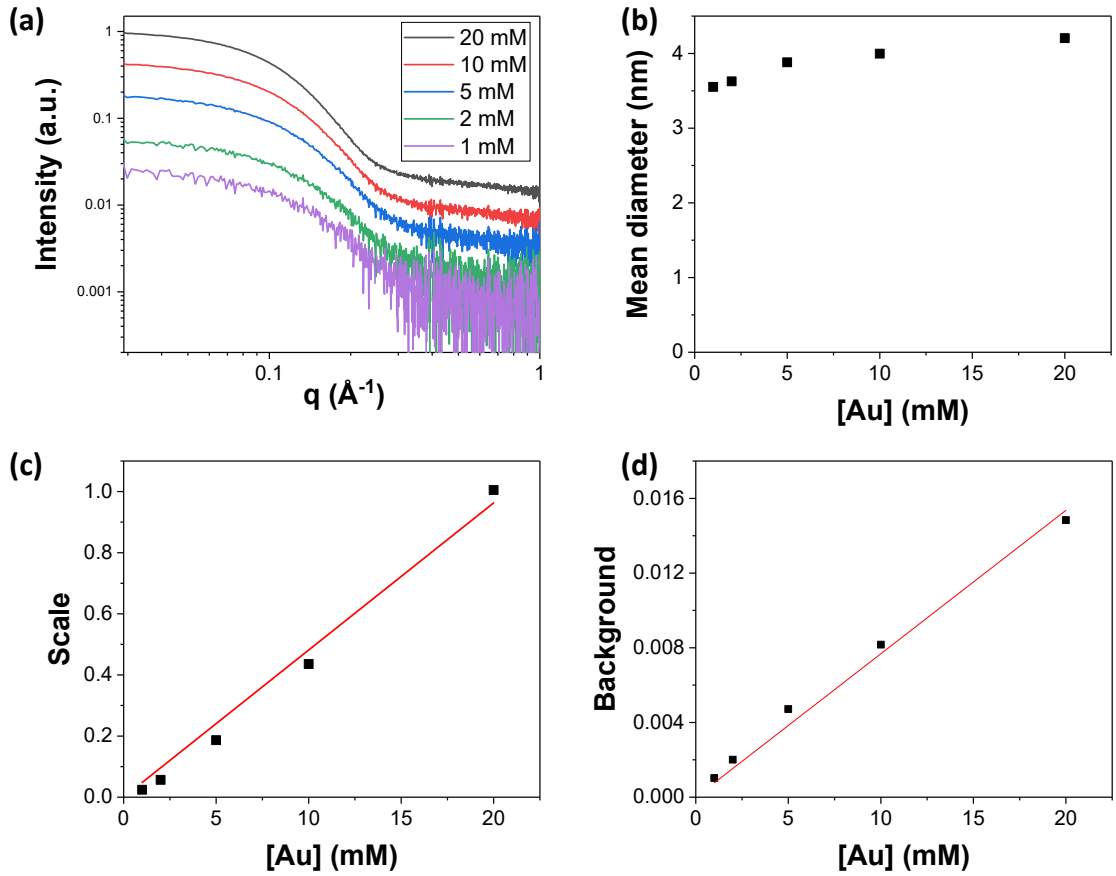

Figure S4. (a) *In situ* SAXS at 25 °C of the Au^{III} clusters obtained by dissolution of $HAuCl_4.3H_20$ in a solution of oleylamine in hexane, the Au concentration was varied from 1 to 20 mM, the molar ratio [OY]/[Au] was kept constant of 2.5; (b) Mean diameter of the Au^{III} clusters at different Au concentrations given by the fit of the SAXS with a Guinier-Porod model (Eq. S1) (*s* and *m* values were found constant and equal to 0 and 4, respectively); Scale (c) and *background* (d) values given by the fits, plotted as a function of the Au nominal concentration.

II.3 Au^{III} clustering assessment

Considering the equilibrium between the free Au^{III} complexes and the Au^{III} clusters denoted hereafter as Au_n^{III}, with *n* the number of Au^{III} complexes involved in one cluster:

$$Au_n^{III} \rightleftharpoons n\, Au^{III} \qquad \text{(Eq. S3)}$$

K_d the dissociation constant writes as:

$$K_d = \frac{[Au^{III}]^n}{[Au_n^{III}]} \qquad \text{(Eq. S3)}$$

The degree of dissociation α is defined as:

$$\alpha = \frac{[Au^{III}]}{c_0} \quad \text{(Eq. S4)}$$

with c_0 the nominal concentration of gold. According to the mass conservation:

$$c_0 = [Au^{III}] + n[Au_n^{III}]$$

And

$$[Au_n^{III}] = \frac{(1-\alpha)}{n} c_0 \quad \text{(Eq. S5)}$$

From the definition of K_d and α, the following relationship can be derived

$$\frac{(c_0)^{n-1}}{K_d} = \frac{1-\alpha}{n.\alpha^n} \quad \text{(Eq. S6)}$$

Equation S6 is generally used to explain that α tends towards 1 when c_0 tends towards zero, i.e. that the dissociation increases with the dilution. In the present case, we do not observe such an effect. With increasing dilution, the size of the clusters remains almost constant (Fig. S4b) which means that n is constant. Moreover, the scale of the Guinier-Porod fit (or the intensity at low q) is proportional to the nominal concentration which means that the volume fraction of the Au^{III} clusters is proportional to the nominal Au concentration. This can be explained by a small degree of dissociation and thus $[Au_n] = \frac{c_0}{n}$, i.e. the totality of the Au^{III} complexes is involved in the Au^{III} clusters. In other words, the dissociation constant, K_d, is very small.

II.4 Density of the Au^{III} clusters

The densities of hexane, a 50 mM solution of OY in hexane, and of the Au^{III} precursor suspension containing $HAuCl_4.3H_2O$ (20 mM) and OY (50 mM) dissolved in hexane are reported in Table S1.

Table S1. Densities of the hexane and various solutions (the measurements were repeated 3 times, the error bar is on the last digit).

Sample	Density ($g.cm^{-3}$)
Hexane	0.6726
OY (50 mM) in hexane	0.6756
$HAuCl_4.3H_2O$ (20 mM) + OY (50 mM) dissolved in hexane	0.6809

Considering that all the $AuCl_4$ solvated by the water molecules are contained in the clusters (there are no free Au^{III} complexes, as discussed above), and according to the mixture rule, the density of the Au^{III} cluster suspension which is considered as nanodroplets containing the Au^{III} complexes and water dispersed in hexane is given by :

$$\rho_{total} = \frac{m_{total}}{V_{total}} \quad \text{(Eq. S7)}$$

$$\rho_{total} = \frac{m_{total}}{\left[\frac{(m_{total} \times X_{cluster})}{\rho_{cluster}} + \frac{(m_{total} \times X_{sol.})}{\rho_{sol.}}\right]} \quad \text{(Eq. S8)}$$

$$\rho_{total} = \frac{1}{\left[\left(\frac{X_{cluster}}{\rho_{cluster}}\right) + \left(\frac{X_{sol.}}{\rho_{sol.}}\right)\right]} \quad \text{(Eq. S9)}$$

where, m_{total}, and V_{total} represent the total mass and volume of the *Au^{III}* suspension, $X_{cluster}$, and $X_{sol.}$ are the mass fractions, and $\rho_{cluster}$, and $\rho_{sol.}$ are the densities, for the PNCs and the solvent, respectively.

Therefore, the density of PNCs is estimated by

$$\rho_{cluster} = \frac{X_{cluster}}{\left[\left(\frac{1}{\rho_{total}}\right) - \left(\frac{X_{sol.}}{\rho_{sol.}}\right)\right]} \quad \text{(Eq. S10)}$$

For [$HAuCl_4.3H_2O$] = 20.0 mM and [OY] = 50.0 mM, the mass fractions are X_{PNCs} = 0.01153 and $X_{sol.}$ = 0.9885. By substituting the density values of Tab. S1 and the mass fractions into Eq. S10, the density of the *Au^{III}* clusters was found to be $\rho_{cluster} =$ 2.07 g.cm^{-3}.

II.5 Assessment of scattering length density of the PNCs

The scattering length density of the *Au^{III}* clusters ($sld_{clsuter}$) was calculated considering that the *Au^{III}* clusters are assemblies of $AuCl_4.3H_2O$ with the density calculated above. Under this assumption the value of $sld_{clsuter}$ = 16.4×10^{-6} Å^{-2} was found. This value is much lower than the *sld* of the Au^0 (sld_{Au} = 126×10^{-6} Å^{-2} for λ = 1.54 Å).

II.6 Assessment of number of gold atoms in each PNC

Using the average size and the density of *Au^{III}* clusters, we can calculate the average mass of the PNCs by :

$$m_{cluster} = \rho_{cluster} * V_{cluster} \quad \text{(Eq. S11)}$$

And we can deduce the average number of gold atoms in each *Au^{III}* cluster by :

$$n_{Au/PNC} = \frac{\rho_{cluster} * V_{cluster}}{M_{AuCl4.3H2O}} \quad \text{(Eq. S12)}$$

where $m_{cluster}$, and $V_{cluster}$ denote the mass and volume, respectively, of each *Au^{III}* cluster. $M_{AuCl4.3H2O}$ refers to the molecular weight of the basic building block of the *Au^{III}* cluster ($AuCl_4.3H_2O$)

Using the average volume is $V_{cluster}$ = 33.5 nm^3 (calculated from the average radius of the *Au^{III}* clusters given by SAXS, r_{PNC} = 2.0 nm, and assuming a spherical shape), the density $\rho_{cluster}$ = 2.07 g.cm^{-3} and M_{AuCl-}

$_{4.3H2O}$ = 393.83 *g/mol*, the average number of gold atoms in each Au^{III} cluster is found to be *ca.* $n_{Au/PNC} =$ 106.

II.7 Calculation of number density of PNC in the precursor suspension

The number density of Au^{III} clusters (number of Au^{III} clusters per cm^{-3}) is given by :

$$ND_{cluster} = \frac{[Au] * N_A}{n_{Au/cluster}} \quad \text{(Eq. S13)}$$

For [Au] = 20 mM = 2.10^{-5} $mol.cm^{-3}$, ND_{PNCs} is found equal to ca. 11.3 10^{16} cm^{-3}.

III. Atomic-scale simulations of the Au^{III} clusters

III.1 Geometry optimizations

Density Functional Theory (DFT) calculations were carried out using the ORCA program version 5.0.[8] Geometry optimizations were performed using the PBE0 hybrid functional[9] in combination with the D4 atom-pairwise and many-body dispersion correction.[10] The optimizations employed the def2-SVP basis set for all atoms, along with the corresponding def2/J auxiliary basis for the resolution-of-identity (RI-J) approximation.[11] The RIJCOSX algorithm[12] was used to accelerate the evaluation of the exact exchange contribution, together with ORCA's default numerical integration grids and *TightSCF* keyword for convergence thresholds. All calculations were carried out using the conductor-like polarizable continuum model (CPCM) solvation model with hexane as the implicit solvent.[13]

III.2 Molecular dynamics calculations

All Molecular dynamics (MD) calculations were performed using the xTB 6.7.1 program[14] with the density functional tight binding GFN2-xTB model.[15] The simulations employed the Analytical Linearized Poisson-Boltzmann (ALPB) implicit solvation model with hexane.[16] Geometry optimizations with default settings were performed prior to 500 ps MD simulations using a Berendsen thermostat at 300K in the NVT ensemble. The SHAKE algorithm was applied during the first 50 ps and subsequently deactivated, while a 2 fs time step was used to improve simulation stability. The systems were confined using the logfermi potential within a spherical region whose radius was automatically determined based on the largest interatomic distance following geometry optimization. The results of the geometry optimizations and MD simulations were analyzed and visualized using the VMD 1.9.4 program.[17]

III.3 System preparation

The initial structures of oleylamine and hydrogen tetrachloroaurate trihydrate were obtained from the PubChem compound database (CIDs 5356789 and 21863413)[18] and subsequently combined to construct the systems used for geometry optimization and molecular dynamics simulations.

Density Functional Theory (DFT) calculations were performed on a complex composed of one $HAuCl_4 \cdot 3H_2O$ and one oleylamine (OY). The molecules were manually positioned using Chimera software,[19] with initial Au-N distances of 3.5 Å and 5 Å.

For MD simulations, the Packmol software[20] was used to build two simulation boxes containing respectively, 5 $HAuCl_4 \cdot 3H_2O$ and 13 OY molecules (803 atoms), and 10 $HAuCl_4 \cdot 3H_2O$ and 25 OY molecules (1550 atoms). The molecules were randomly distributed within cubic boxes with edge lengths of 20 and 25 Å, as shown in Figures S5 a and b, respectively.

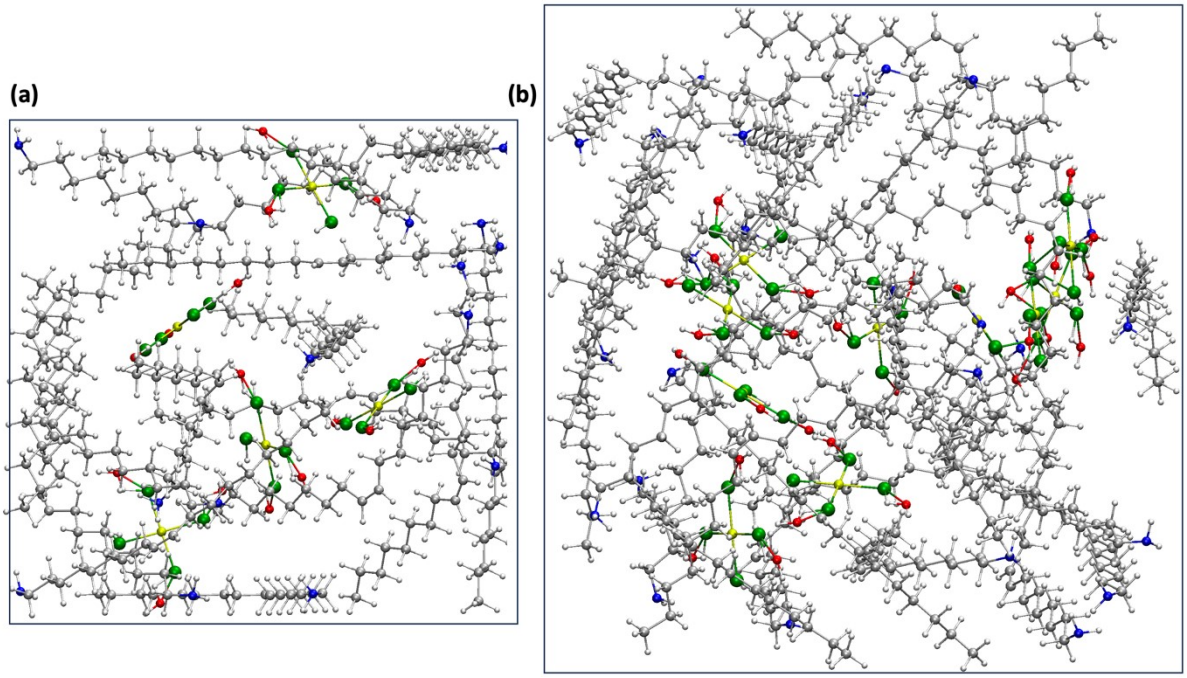

Figure S5. The Packmol software was used to construct two simulation boxes, respectively with (a) 5 $HAuCl_4 \cdot 3H_2O$ and 13 OY (915 atoms) and (b) 10 $HAuCl_4 \cdot 3H_2O$ and 25 OY molecules (1550 atoms).

III.4 Interactions between $HAuCl_4$-$3H_2O$ with oleylamine

Density Functional Theory (DFT) calculations were performed on a complex composed of one $HAuCl_4 \cdot 3H_2O$ and one oleylamine (OY) molecule to investigate their possible interaction modes. Two initial modes were used with Au-N distances of 3.5 Å and 5 Å. The two optimized structures highlight two distinct mechanistic pathways governing the early-stage interaction between oleylamine (OY) and $HAuCl_4 \cdot 3H_2O$. These pathways differ in the sequence of proton transfer, ligand exchange, and approach of the amine group.

Direct amine coordination followed by HCl formation (Figure S6a). When oleylamine is initially placed within short range of the Au^{III} center (Au–N = 3.5 Å), the interaction is dominated by the nucleophilic character of the amine. This coordination event weakens a nearby Au-Cl bond and results in HCl formation. The final geometry features an Au-N bond of 2.05 Å and a planar coordination environment in which Au–Cl bond lengths are consistently 2.30 Å.

Proton transfer and ion pair formation prior to Au–N contact (Figure S6b). When the initial Au–N distance is larger (5 Å), direct nucleophilic attack becomes less favorable. Instead, proton transfer occurs from hydrated $HAuCl_4$ to the amine, generating an oleylammonium ion and a tetrachloroaurate ion. The Au^{III} center remains exclusively coordinated to four chloride ligands, preserving a square-

planar $AuCl_4^-$ geometry, while the water molecules reorganize to stabilize the ion pair and mediate long-range interactions.

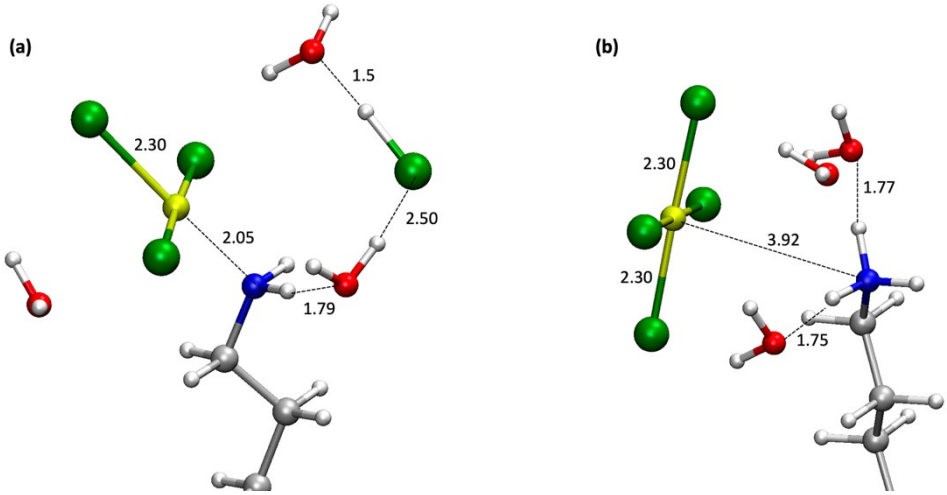

Figure S6. Structures obtained after DFT geometry optimization starting from two different initial models (Color code: red: O, white: H, blue: N, yellow: Au, green: Cl): (a) An initial Au-N distance of 3.5 Å leads to HCl formation, with the nitrogen atom of oleylamine coordinating directly to the Au^{III} center; (b) An initial Au-N distance of 5 Å results in the formation of an oleylammonium ion and a tetrachloroaurate ion.

The two optimized structures differ in energy by 0.68 eV, with the ion-pair configuration (Figure S6b) being thermodynamically more stable. Mechanistically, close initial contact between oleylamine (OY) and $HAuCl_4{\cdot}3H_2O$ favors the direct amine coordination to the Au^{III} center, followed by HCl formation (Figure S6a). At larger initial separations, proton transfer occurs first, yielding an oleylammonium / tetrachloroaurate ion pair (Figure S6b).

Despite this difference in energy, both pathways are kinetically accessible and expected to occur under realistic conditions. Solvent motions and other dynamical events can bring the amine close enough to the Au^{III} center to promote direct binding, even if this state is not the global minimum. This coexistence of mechanistic pathways is further investigated through molecular dynamics simulations.

III.5 Dynamical evolution of $HAuCl_4$-$3H_2O$ in solution of oleylamine in hexane

Semi-empirical MD simulations were performed on larger systems to follow molecular diffusion while accounting for possible proton transfers, and bond formation or cleavage. For clarity, we present the results in detail for the smallest simulation box and illustrate the final configuration obtained for the largest box.

During the early stages of optimization, the events previously characterized by DFT calculations are reproduced. Figure S7 shows the optimized structure for the smallest simulation box (5 $HAuCl_4{\cdot}3H_2O$), highlighting an Au^{III} ion coordinated to three chloride ions and one nitrogen atom from a neighboring oleylamine molecule (Fig. S7b). A proton transfer from HCl to the amine is also observed, mediated indirectly by two water molecules (Fig. S7c). These results demonstrate that xTB accurately reproduces the key events identified by DFT, supporting the reliability of subsequent MD simulations.

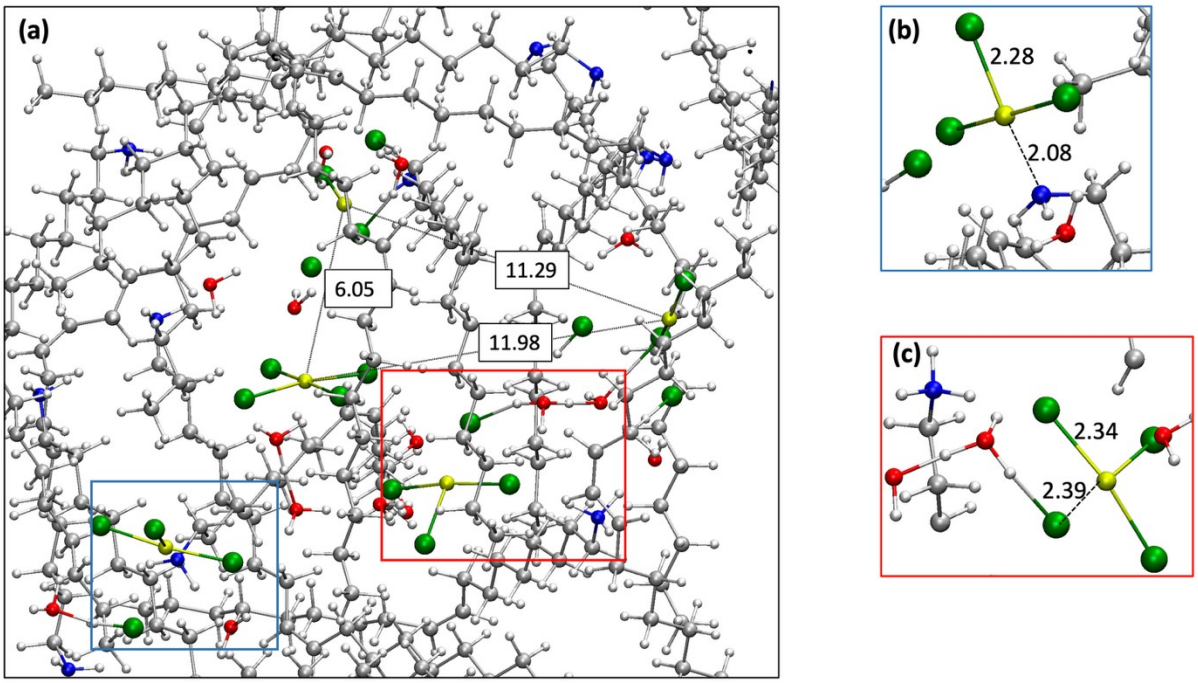

Figure S7. Arrangement obtained after geometry optimization of the small box (5 $HAuCl_4 \cdot 3H_2O$). Selected Au^{III}-Au^{III} distances are reported, showing that these atoms are still separated by at least 6 Å. Two regions reproducing the configurations observed in DFT are highlighted: the blue box in (b) corresponds to the configuration of Fig. S6a, and the red one in (c) to the configuration of Fig. S6b.

During the first 50 ps of the trajectory, water molecules diffuse between tetrachloroaurate ions and form bridging interactions as the ions approach each other. Figure S8 shows a snapshot of the trajectory after 50 ps of simulation, where Au^{III} are separated by approximately 7 Å.

After 500 ps of simulation, a stable gold chloride core surrounded by a shell of nitrogen atoms from oleylamine and oleylammonium ions is obtained. Figure S9a shows a close-up of this core, where the 13 nitrogen atoms in the simulation box are clearly visible within the local environment. Amine and ammonium groups interact through hydrogen bonds. Water molecules diffuse around the core or form small clusters in the outer shell, which contains disordered alkyl chains from oleylamine and oleylammonium. Figure S9b presents an alternative view of the core. For clarity, Figure S9c highlights selected atoms, showing that Au^{III} ions are mostly coordinated to four chloride ligands, while one is coordinated to three chloride ions and one nitrogen atom from an oleylamine. The atoms are arranged so that the $AuCl_4^-$ planes form square bases of pyramidal or bipyramidal motifs, with the apex defined by a chloride atom from an adjacent plane.

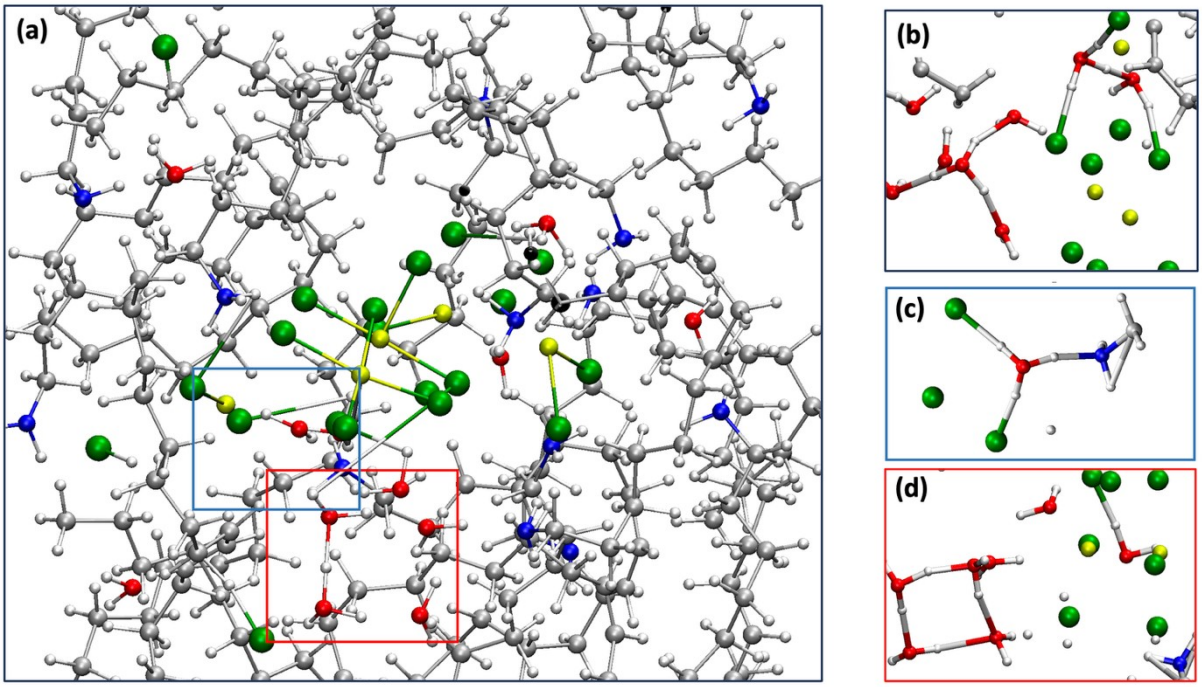

Figure S8. (a) Structure obtained after the first 50 ps of MD simulations, showing Au^{III} ions approaching each other via interactions mediated by water molecules; (b) Box highlighting an event representative of those occurring during the initial tens of picoseconds of the trajectory; (c) and (d) Zoomed-in views of panel (a), (c) illustrates a water-mediated proton transfer from HCl to an amine group, with the water molecule bridging two chloride ions and (d) shows the formation of a small cluster of water molecules.

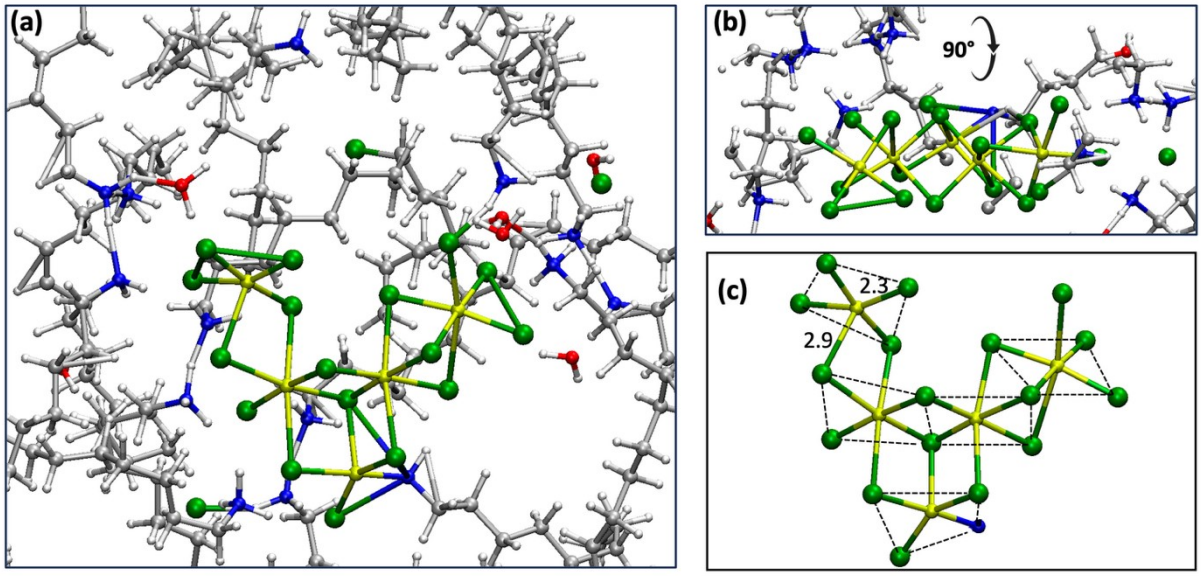

Figure S9. (a) Close-up of the gold–chloride core after 500 ps, surrounded by nitrogen atoms from oleylamine and oleylammonium, with hydrogen-bonded amine and ammonium groups. (b) View (b) shows the configuration after a 90° rotation relative to view (a). (c) Selected atoms highlighting that most Au^{III} ions are coordinated to four chloride ligands, except one coordinated to three chloride ions

and one nitrogen atom from oleylamine. Dashes are used to visualize the square-planar $AuCl_4^-$ geometry. Au-Cl distances are indicated in angstrom.

The same protocol was applied to the largest box (10 $HAuCl_4 \cdot 3H_2O$ and 25 OY molecules). As shown in the Figure S10, these calculations lead to similar observations throughout the trajectory. During the first 100 ps of the simulation, we observe the formation of two small Au^{III} clusters, closely resembling the one previously described, stabilized by water-mediated interactions, with amine and ammonium groups beginning to form a surrounding shell. By the end of the simulation, an organized gold-chloride core has formed, encircled by nearby nitrogen atoms, while water molecules diffuse through the oleylamine alkyl chains.

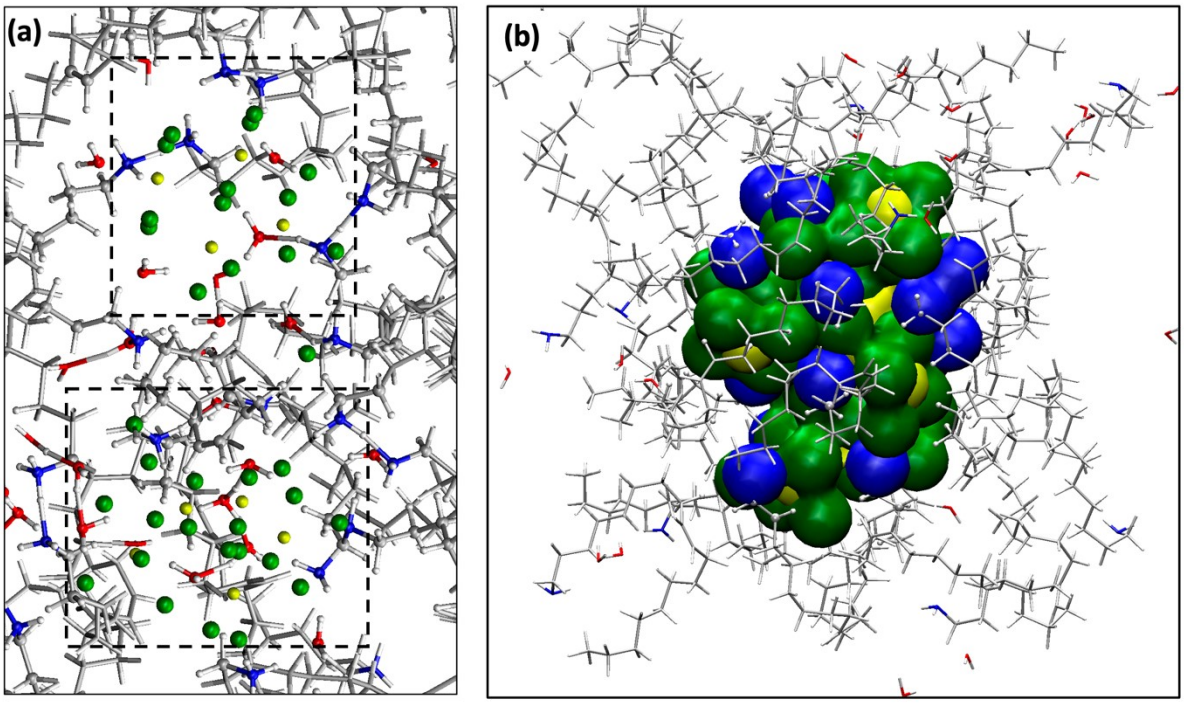

Figure S10. (a) Two small Au^{III} clusters form in the early stage of the simulations, stabilized by water-mediated interactions and hydrogen bonds involving nearby amine and ammonium groups; (b) by the end of the simulation a stable gold-chloride core has been obtained.

IV. SAXS analysis of the Au nanoparticles

The SAXS of the Au NP suspensions prepared by reduction of the Au^{III} precursor suspensions were analyzed using the software SasView 5.0.5 with the sum of two form factor of spheres[21] with polydispersity described by a Schulz distribution, and an incoherent contribution (*background* contribution) (Eq. S14).

$$I(q) = \left[\frac{scale_A}{V_A}\left[3V_A(\Delta\rho).\frac{\sin(qr_A) - qr_A cos(qr_A)}{(qr_A)^3}\right]^2 + \frac{scale_B}{V_B}\left[3V_B(\Delta\rho).\frac{\sin(qr_B) - qr_B co}{(qr_B)^3}\right.\right.$$

(Eq. S14)

where $scale_A$ and $scale_B$ are the volume fractions, V_A and V_B the volumes, r_A and r_B the radii of the of the population A and B, respectively. *background* is the background level constant all over the q range. $\Delta\rho$ is the difference between the scattering length densities (*sld*) of the Au NPs and the solvent, $\Delta\rho = sld_{Au} - sld_{hexane}$. SLD of 126 10^{-6} Å^{-2} and 6.5 10^{-6} Å^{-2} were taken for Au and hexane, respectively.

For the fitting, the scales, radii and polydispersity of population A and B, and the background level were adjustable parameters. The results of the SAXS fitting for four suspensions prepared with different concentrations of reducing agent are presented Figure S11.

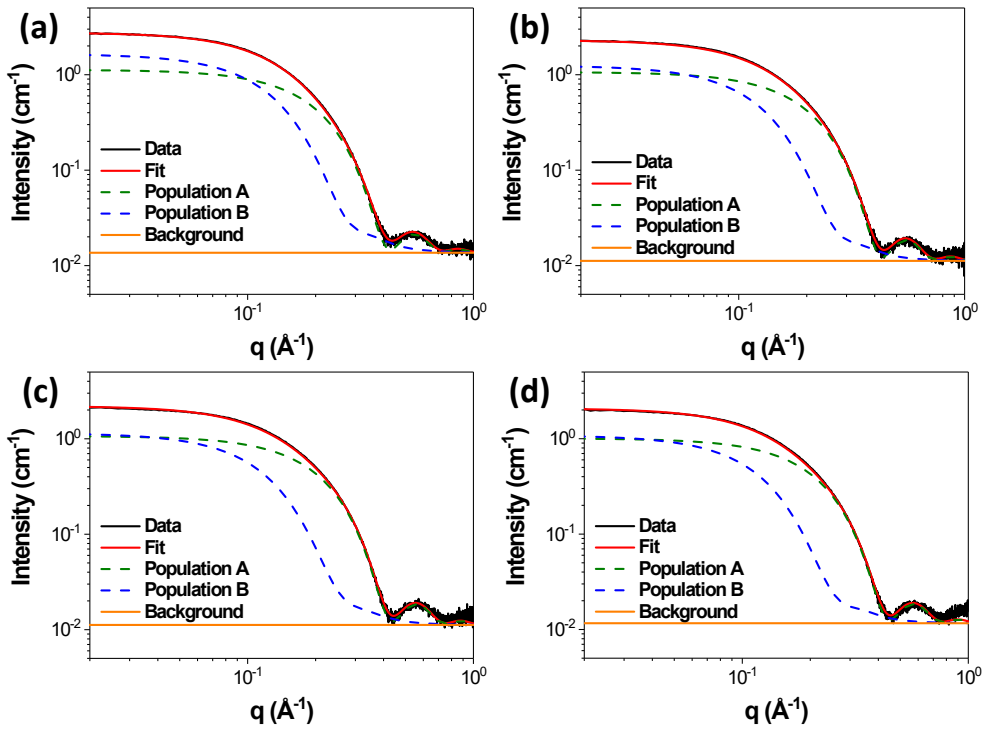

Figure S11. SAXS of Au NP suspensions prepared by reduction of $HAuCl_4.3H_2O$ in a solution of OY in hexane ([Au] = 20 mM; [OY]/[Au] = 2.5) using TES as reducing agent in different concentrations (a) [TES]= 62 mM; (b) [TES]= 125 mM; (c) [TES]= 250 mM; (d) [TES]= 500 mM. Experimental data (black), best fits including two populations of nanospheres (red), population A (dashed blue), population B (dashed green), and background (orange).

The SAXS data of Au NPs suspensions prepared by reduction of Au^{III} solutions with different [Au] concentration in the range 2-20 mM using a large excess of TES ([TES] = 500 mM) are given Fig. S12a. The radii and % in number of the two Au NP populations obtained by fitting the SAXS with Eq. S14 are plotted in Fig. S12b,c. Regardless of the gold concentration, population A with a radius of ca. 10 Å constitutes the large majority and population B with a radius of 15 Å is only a very small minority.

The relation between the volume fraction and the gold concentration is given by :

$$\%vol.Au = [Au] \times \frac{M_{Au}}{\rho_{Au}} \qquad \text{(Eq. S15)}$$

with M_{Au} and ρ_{Au}, the molecular weight and density of Au.

Taking M_{Au} = 197 g.mol^{-1} and ρ_{Au} = 19.3 g.cm^{-3}, theoretical values of *% vol. Au* are 2.10^{-5} and 2.10^{-4} for [Au] = 2 mM and 20 mM, respectively.

The experimental total Au NPs volume fraction, *% vol. Au* = $scale_A$ + $scale_B$, is plotted as a function of the initial Au concentration (Fig. S12d). It varies linearly between 2×10^{-5} and 2×10^{-4} for [Au] ranging between 2 and 20 mM. showing that the yield of reduction is 100 % regardless of the initial Au concentration

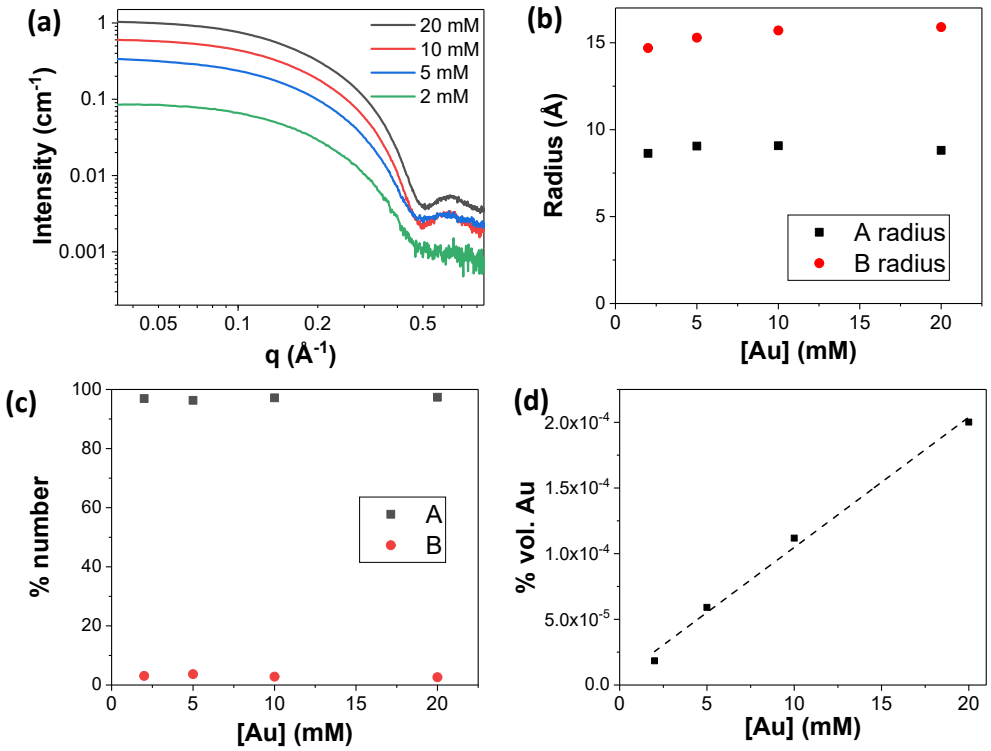

Figure S12. (a) SAXS of Au NP suspensions prepared by reduction with TES ([TES] = 500 mM) of $HAuCl_4.3H_2O$ dissolved in OY/hexane ([OY]/[Au] = 2.5), at different Au concentrations in the range 2 – 20 mM ; (b-d) Results of the SAXS fitting with two populations of spheres A and B: (b) mean particle diameters, (c) relative proportion of both populations in number and (d) total volume fraction plotted as a function of [Au].

V. Atomic structure – PDF analysis

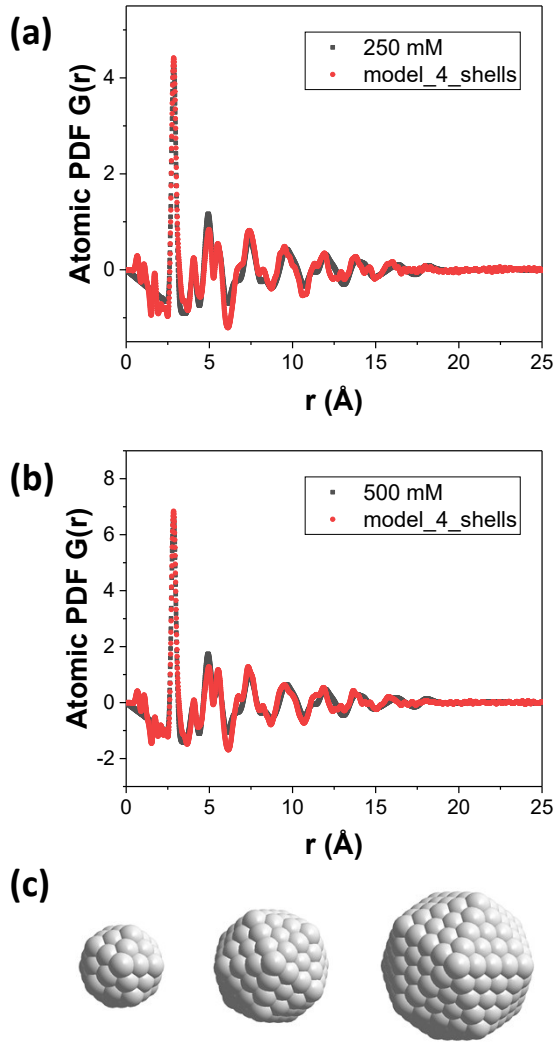

Figure S13. Experimental atomic PDF (black) of the particles prepared with (a) [TES]= 250 mM and (b) [TES] = 500 mM. Calculated PDF (red) of a 4-shells icosahedral model and 4-shell icosahedron model shown as inset. (c) 2-, 3-, and 4-layer icosahedral models, with 55, 147, and 309 atoms, and sizes of 1.1, 1.6, and 2.15 nm, respectively.

VI. Time-resolved XAS analysis

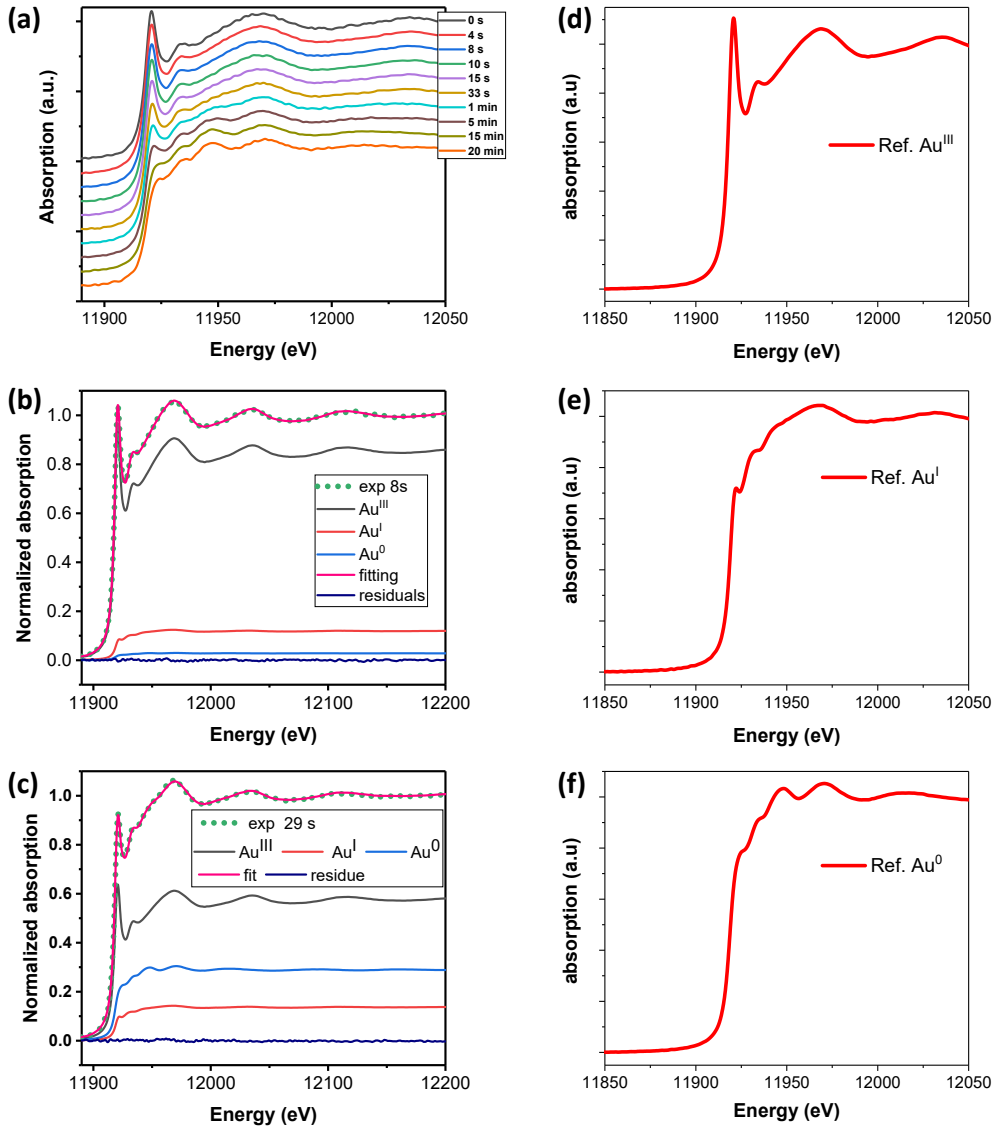

Figure S14. *Left panel*. (a) *In situ* XAS spectra at the Au L_{III}-edge recorded during the reduction of $HAuCl_4.3H_2O$ in OY/hexane ([Au] = 20 mM ; [OY] = 50 mM) with [TES] = 62 mM ; XAS spectra (open circle) at 8s (b) and 29 s (c) fitted by a linear combination of three components (magenta line), Au^{III} , Au^{I} and Au^{0} contributions in black, red and blue, respectively.

Right panel. *In situ* XAS spectra at the Au L_{III}-edge of the three references used for the linear combination analysis: (d) Au^{III} ; (e) Au^{I} ; (f) Au^{0}.

Preparation of the three references:

(d) Solution containing 20 mM $HAu^{III}Cl_4.3H_2O$ and 50 mM OY freshly dissolved in hexane;

(e) Lamellar phase OY-Au^{I}-Cl in suspension in hexane. 20 mg of HAuCl4,3H2O were dissolved in 2.5 mL of pure oleylamine under ultrasonication (15 min). The solution was then kept undisturbed at 25°C for 48 h, leading to the formation of a white precipitate. The white precipitate was separated form the supernatant by centrifugation and redispersed in a several tens microliters of hexane to fill the capillary. Chemical and WAXS characterizations showed a molar ratio Au/Cl = 1 and an interlayer spacing of 48 Å, in agreement with previous publications.[22,23] It should be noted that the presence of excess free OY in the suspension has no effect on the gold edge.

(f) Metal Au^0 nanoparticles prepared by reduction of the precursor solution with a large excess of TES.

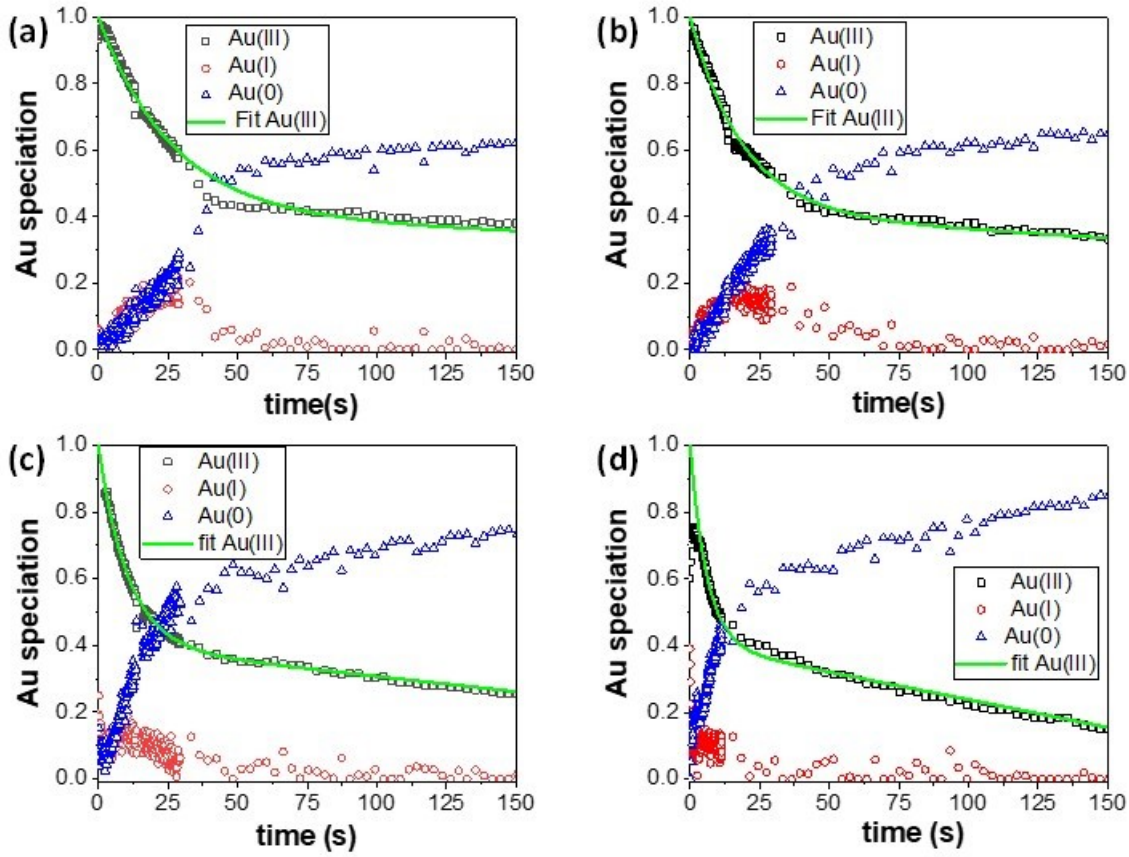

Figure S15. Relative Au^{III}, Au^{I} and Au^0 concentrations deduced from the linear combination analysis of the XAS spectra measured *in situ* during the reaction with (a) [TES] = 62 mM; (b) [TES] = 125 mM; (c) [TES] = 250 mM; (d) [TES] = 500 mM.

The green lines are the best fit of $[Au^{III}]$ using Eq. S16:

$$[Au^{III}] = [Au^{III}]_i + \left(1 - [Au^{III}]_i\right) exp(-kt) - k't \quad \text{(Eq. S16)}$$

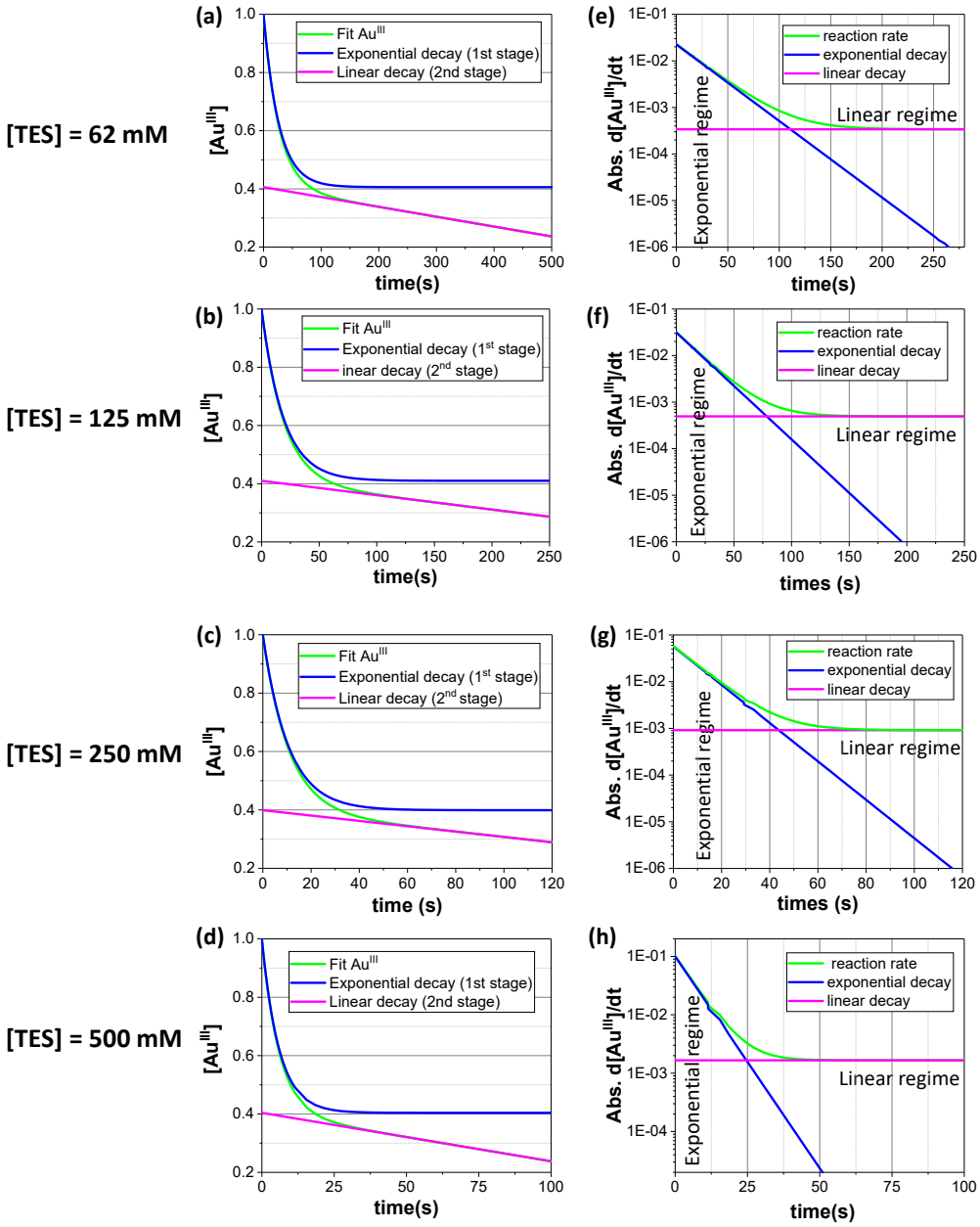

Figure S16. Best fit of the [Au^{III}] decay (green line) for Au synthesis performed with (a) [TES] = 62 mM; (b) 125 mM; (c) 250 mM; (d) 500 mM. Fits were done using Eq. S16 and compared with the exponential decay only of Eq. S17 (blue line) and with the linear decay only of Eq. S18 (magenta line). It illustrates that Eq. S17 fits the short times and Eq. S18 the long times; (e-h) Derivatives of the 3 curves showing that the linear decay becomes faster than the exponential decay at t_2^* = 106 s, 78 s, 44 s and 25 s for [TES] = 62 mM, 125 mM, 250 mM and 500 mM, respectively.

$$[Au^{III}] = [Au^{III}]_{int.} + \left(1 - [Au^{III}]_{int.}\right) exp(-kt) \quad \text{(Eq. S17)}$$

$$[Au^{III}] = [Au^{III}]_{int.} - k't \quad \text{(Eq. S18)}$$

The time t_1^* at which $[Au^{III}] = [Au^{III}]_{int.}$ solution of the equation $k't_1^* = \left(1 - [Au^{III}]_{int.}\right) exp\left(-kt_1^*\right)$ was determined graphically. The time t_2^* was calculated according to $t_2^* = \frac{1}{k} Ln\left[\frac{k}{k'}\left(1 - [Au^{III}]_{int.}\right)\right]$. The values of t_1^* and t_2^* for the different TES concentrations are reported Tab. S2.

Table S2. Parameters of the best fits of the [Au^{III}] time dependence using (Eq. S16) and characteristic times t_1^* and t_2^* at which $[Au^{III}] = [Au^{III}]_{int.}$ and at which the linear decay becomes faster than the exponential one, respectively.

[TES] (mM)	$[Au^{III}]_{int}$	***k*** **(s^{-1})**	***k'*** **(s^{-1})**	t_1^* **(s)**	t_2^* **(s)**
62	0.411	3.87 10^{-2}	3.71 10^{-4}	75	106
125	0.410	5.29 10^{-2}	4.94 10^{-4}	57	78
250	0.399	9.47 10^{-2}	9.16 10^{-4}	32	44
500	0.404	16.8 10^{-2}	16.6 10^{-4}	18	25

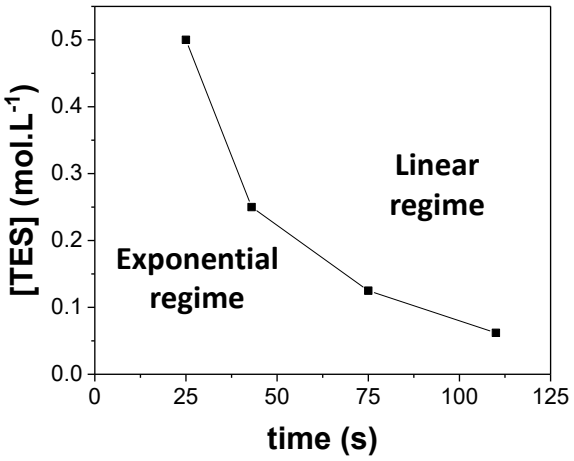

Figure S17. Critical time, t_2^*, above which the linear regime becomes faster than the exponential regime plotted for the different TES concentrations.

VII. Time-resolved SAXS analysis

VII.1. Initial SAXS

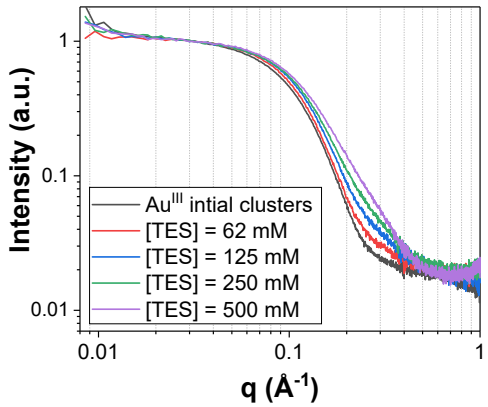

Figure S18. Comparison of the SAXS pattern of the Au^{III} clusters suspension before and after 300 ms of reaction following the addition of TES at different concentrations. Additional signal around 0.3 $Å^{-1}$ is due to the scattering intensity of the first Au^0 nanoparticles.

VII.2. SAXS fitting method

The strategy for analyzing the SAXS data was as follows.

We started from the end of the reaction, for which it had been shown that the scattering intensity I(q) resulted from a majority population of 2 nm particles and a very small minority population of larger particles. The time-resolved SAXS were analyzed using SASVIEW with a sum of two form factors of polydisperse spheres, noted A and B. For each population of spheres the polydispersity were described by a Schulz distribution. In this analysis population A corresponds to the smallest NPs and population B to the biggest.

$$I(q) = \left[\frac{scale_A}{V_A}\left[3V_A(\Delta\rho).\frac{\sin(qr_A) - qr_A cos(qr_A)}{(qr_A)^3}\right]^2 + \frac{scale_B}{V_B}\left[3V_B(\Delta\rho).\frac{\sin(qr_B) - qr_2c}{(qr_B)^3}\right.\right.$$

(Eq. S19)

The parameters $scale_A$ and $scale_B$ are the unitless volume fraction of each population, V_A and V_B the NP volume. The ratio $ND_A = \frac{scale_A}{V_A}$ and $ND_B = \frac{scale_B}{V_B}$ are the number density, expressed in cm^{-3}. $\Delta\rho$ is the difference between the scattering length density (*sld*) of the nanoparticles and the solvent.

The fitting parameters were the scale factors, $scale_A$ and $scale_B$, the radii, R_A and R_B, the polydispersity ratio of the Schulz distribution, PD_A and PD_B, and the background value.

The *sld* of hexane was fixed at 6.5 10^{-6} $Å^{-2}$, value calculated for the X-ray energy of 12 keV.

The *sld* of population A and B was fixed at 118×10^{-6} $Å^{-2}$, i.e. the *sld* value of metal gold for the X-ray energy of 12 keV. These values fitted correctly the final SAXS.

Then, the time-resolved SAXS were then analyzed from the end and going backward in time using Eq. S19 and the same *sld* values, i.e. considering a mixture of two populations of Au^0 spheres. This model should describe the experimental data at the end of the reaction, but should fail at the beginning of the reaction when the initial Au^{III} clusters contributes to the scattered intensity. In order to determine the time at which the Au^{III} clusters disappeared and when the scattering signal was only due to the two populations of Au^0 NPs, the total molar Au^0 concentration was calculated from the sum of the volume fractions of both populations given by the SAXS fitting following:

$$[Au^0] = \frac{(scale_A + scale_B) \times \rho_{Au}}{M_{Au}} \qquad \text{(Eq. S20)}$$

with M_{Au} = 197 $g.mol^{-1}$ and ρ_{Au} = 19.3 $g.cm^{-3}$ the molecular weight and density of gold.

According to Eq. S19, the volume fractions of each population determined by the fits depend on $\Delta\rho$, i.e. on the choice of the *sld* of the corresponding population and of the solvent. Using the *sld* value of gold (118×10^{-6} $Å^{-2}$) for populations A and B, the total [Au^0] value given by Eq. S20 will correspond to the value determined by XAS if the scattering intensity comes solely from metal particles. By contrast, if a significant contribution to the scattering intensity arises from the initial Au^{III} clusters, this [Au^0] value will be overestimated.

Figure S19 shows the normalized values of [Au^0] calculated from the SAXS fitting (Eq. S19 and S20), which are compared with the [Au^0] values deduced from the XAS analysis previously reported Figs. 3 and S15, for the experiments with different TES concentrations. The agreement between the two curves is excellent for the second stage of the reaction. For this stage, it is thus possible to consider only two populations of gold NPs as scattering objects. The Au^{III} clusters that are the main population of scattering objects at t = 0 are no more present in the suspension at the end of the first stage. On the other hand, a clear discrepancy between the two curves is noticeable for the first stage (Insets in Fig. S19). For the shorter times, the Au^0 concentration calculated from the SAXS fitting using Eqs. 19 and 20 was overestimated. For this time range, we can conclude that a significant contribution of the SAXS signal comes from Au^{III} clusters still present.

Comparison of the SAXS and XAS data therefore allows us to conclude that:
- The Au^{III} clusters are present throughout the first stage while their contribution to the scattered intensity becomes negligible in the second stage. The time at which the Au^{III} clusters determined by SAXS is in good agreement with the time at which the kinetics regime described by XAS switches from the first to the second stage.

- For the second stage, the linear variation in [Au^0] concentration was determined by two independent techniques involving different physical properties (X-ray absorption or scattering). The excellent agreement at longer times between XAS and SAXS shows the reliability of the linear growth of [Au^0] during the second phase of the reaction.

Fitting the SAXS data of the first stage of the reaction was challenging since, as mentioned above, three constituents could coexist in suspension, Au^{III} clusters together with small and big Au^0 NPs, that dramatically increased the number of fitting parameters. An alternative is to considering only the two populations of Eq. S19. Population A refers to the smallest NPs in the reaction medium. These are the very first Au^0 NP that appear at short times in the initial suspension of Au^{III} clusters. They then become the main population in the final suspensions. Population B refers the largest particles in suspension. These particles can be the Au^{III} clusters present at short times or the biggest Au^0 NPs at longer times or a mixture of both for the intermediate time range. The choice of the *sld* of population B only affects the volume fraction and number density of this population but does not contribute neither to the signal of population A nor to the size of the population B. Since the SAXS signal of the smallest Au^0 NPs (population A) appears in a q-range that is significantly shifted from that of the biggest ones, the results of the fit using Eq. 19 for this population can be considered as independent of the choice of the *sld* of population B and therefore reliable.

Fig. 6 and Fig. S20 show the variation over time in the number density (ND_A), radius (R_A) and polydispersity ratio of the Schulz distribution (PD_A) of population A given by fitting the SAXS curves for different [TES].

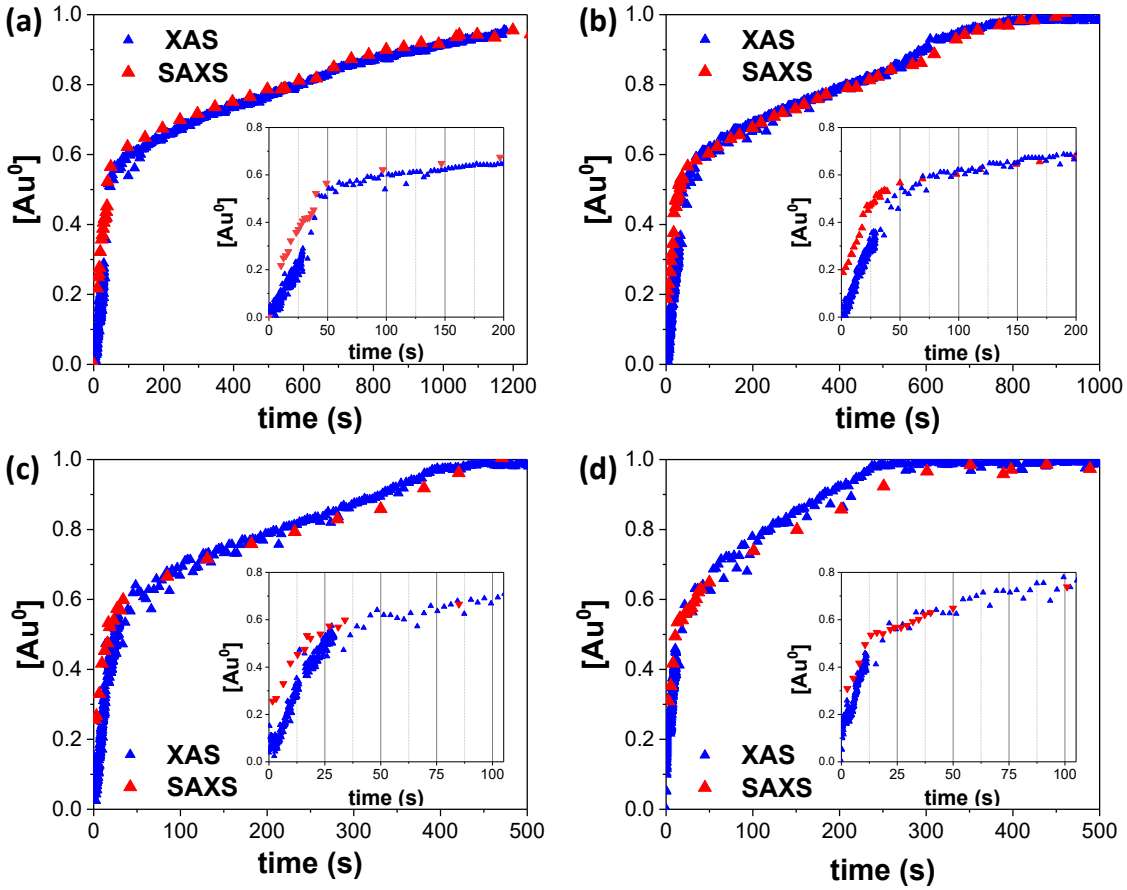

Figure S19. [Au^0] calculated from the fitting of the SAXS considering two populations of Au^0 spheres (red) and from the fitting of the XAS data (blue), for the reactions with [TES] = 62 mM (a); 125 mM (b); [TES] = 250 mM (c) and ; 500 mM (d). *Inset*: zoom on the first stages.

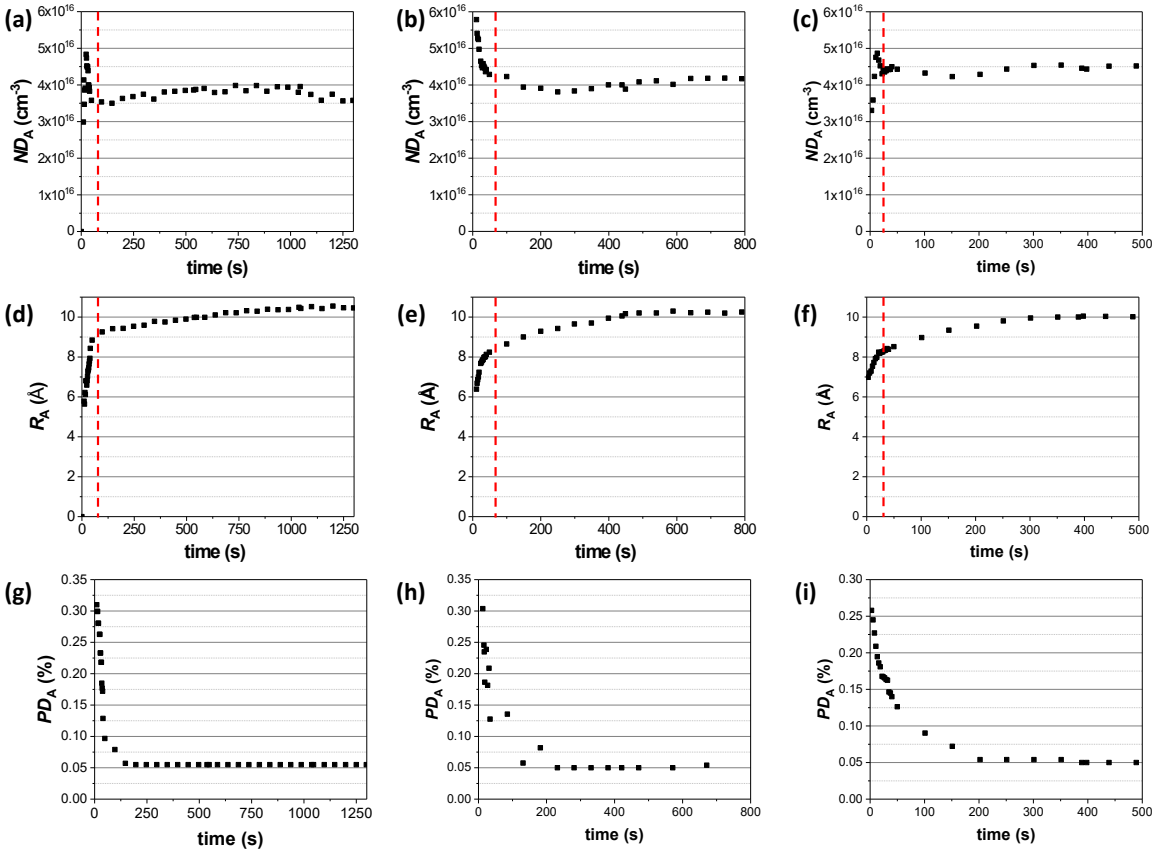

Figure S20. Number density (ND_A), radius (R_A) and polydispersity (PD_A) vs time of the major population of Au^0 NPs given by the fitting of the time-resolved SAXS measured during the reduction with [TES] = 62 mM (a, d, g) ; [TES] = 250 mM (b, e, h)); [TES] = 500 mM (c, f, i). The dashed red line highlights the end of nucleation, time at which the number density becomes constant.

VII.3. SAXS comparison of spheres and icosahedra

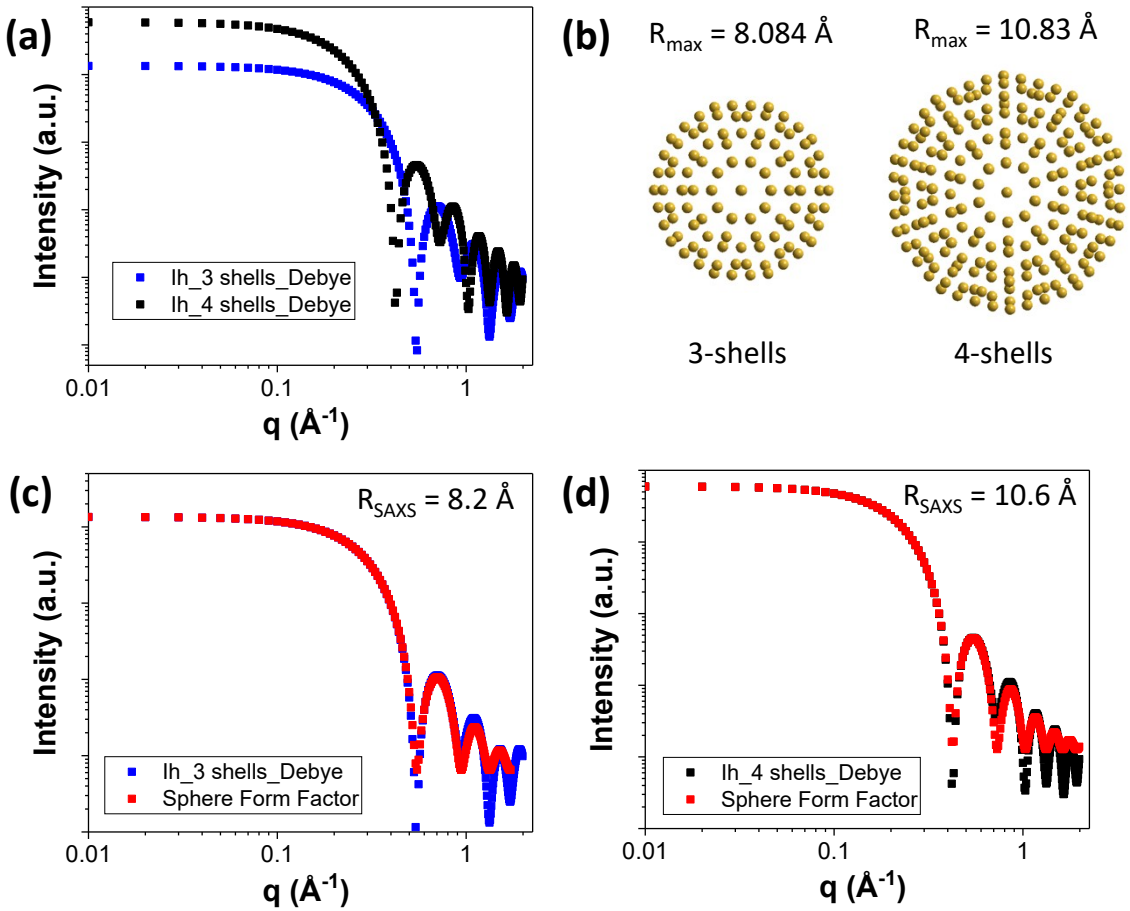

Figure S21. (a) SAXS of 3- and 4-shells icosahedra calculated using the Debye equation and (b) the corresponding models with R_{max} the longest inter-atomic distance between the central atom and the atoms localized at a kink; (c) and (d) best fits with a sphere form factor of the 3- and 4-shells icosahedra SAXS using SASVIEW and corresponding radii given by the fits.

VIII. Kinetic modelling of the 2nd stage

Surface reaction is the rate determining step

For the modelling the growth only stage (2nd stage), the following sequence of elementary reactions has been defined:

$$Au_{sol.}^{III} + S \underset{k_{-1}^{'}}{\overset{k_1^{'}}{\rightleftarrows}} Au_{ads.}^{III} \quad \text{(Eq. S21)}$$

$$Au_{ads.}^{III} + TES \xrightarrow{k_2^{'}} Au_{ads.}^{I} \quad \text{(Eq. S22)}$$

$$Au_{ads.}^{I} + \frac{1}{2}TES \xrightarrow{k_3^{'}} Au^0 + S \quad \text{(Eq. S23)}$$

Eq. S1 describes the equilibrium between the Au^{III} complexes in solution, $Au_{sol.}^{III}$, and the ones adsorbed at the surface of the primary Au NPs, $Au_{ads.}^{III}$, *S* defines an unoccupied adsorption site at the surface of the particles. Eq. S22 describes the reduction of the adsorbed species into adsorbed $Au_{ads.}^{I}$, with one equivalent of TES. Eq. S23 describes the reduction of $Au_{ads.}^{I}$ into Au^0 which releases at the same time an unoccupied site.

According to Eqs.S21-S23, the following rates can be defined:

$$-\frac{d\left[Au_{sol.}^{III}\right]}{dt} = k_1^{'}[S]\left[Au_{sol.}^{III}\right] - k_{-1}^{'}\left[Au_{ads.}^{III}\right] \quad \text{(Eq. S24)}$$

$$-\frac{d\left[Au_{ads.}^{III}\right]}{dt} = -k_1^{'}[S]\left[Au_{sol.}^{III}\right] + k_{-1}^{'}\left[Au_{ads.}^{III}\right] + k_2^{'}\left[Au_{ads.}^{III}\right][TES] \quad \text{(Eq. S25)}$$

$$-\frac{d\left[Au_{ads.}^{I}\right]}{dt} = -k_2^{'}\left[Au_{ads.}^{III}\right][TES] + k_3^{'}\left[Au_{ads.}^{I}\right][TES]^{1/2} \quad \text{(Eq. S26)}$$

$$\frac{d\left[Au^0\right]}{dt} = k_3^{'}\left[Au_{ads.}^{I}\right][TES]^{1/2} \quad \text{(Eq. S27)}$$

During the 2nd stage:

$$-\frac{d\left[Au_{ads.}^{I}\right]}{dt} = 0 \quad \text{and} \quad \frac{d\left[Au^0\right]}{dt} = -\frac{d\left[Au_{tot.}^{III}\right]}{dt}$$

so:

$$k_2^{'}\left[Au_{ads.}^{III}\right][TES] = k_3^{'}\left[Au_{ads.}^{I}\right][TES]^{1/2} \quad \text{(Eq. S28)}$$

and

$$-\frac{d\left[Au_{tot.}^{III}\right]}{dt} = k_2^{'}\left[Au_{ads.}^{III}\right][TES] \quad \text{(Eq. S29)}$$

A fast equilibrium between $Au_{sol.}^{III}$ and $Au_{ads.}^{III}$ implies that:

$$\frac{\left[Au_{ads.}^{III}\right]}{[S]\left[Au_{sol.}^{III}\right]} = \frac{k_1^{'}}{k_{-1}^{'}} \quad \text{(Eq. S30)}$$

and

$$\frac{d\left[Au^0\right]}{dt} = k_2^{'}[TES]\frac{k_1^{'}}{k_{-1}^{'}}[S]\left[Au_{sol.}^{III}\right] \quad \text{(Eq. S31)}$$

In this condition, the total concentration of adsorption sites, S_0, is given by:

$$S_0 = [S] + \left[Au_{ads.}^{III}\right] = [S]\left(1 + \frac{k_1^{'}}{k_{-1}^{'}}\left[Au_{sol.}^{III}\right]\right) \quad \text{(Eq. S32)}$$

$$\frac{d\left[Au^0\right]}{dt} = k_2^{'}[TES]S_0 \times \frac{\frac{k_1^{'}}{k_{-1}^{'}}\left[Au_{sol.}^{III}\right]}{1 + \frac{k_1^{'}}{k_{-1}^{'}}\left[Au_{sol.}^{III}\right]} \quad \text{(Eq. S33)}$$

If the proportion of unoccupied sites is very small, $[S] \ll \left[Au_{ads.}^{III}\right]$, according to Eq. S30:

$$1 \ll \frac{k_1}{k_{-1}}\left[Au_{sol.}^{III}\right]$$

and the reaction rate writes as:

$$\frac{d\left[Au^0\right]}{dt} = -\frac{d\left[Au_{tot.}^{III}\right]}{dt} = k_2^{'}[TES]S_0 \quad \text{(Eq. S34)}$$

If these conditions are fulfilled, the reaction rate is of 1st order with respect to TES and zero-order with respect to Au^{III}.

Diffusion of TES is the rate determining step

Another condition lead to a zero-order reaction with respect to Au^{III} and 1st order with respect to TES. The reduction of the $Au_{ads.}^{III}$ described by Eq. S22 can be split in two elementary reactions, the diffusion of TES from the solution to the primary particle surface (Eq. S22a) and the reaction of TES and $Au_{ads.}^{III}$ at the surface (Eq. S22b) :

$$TES_{sol.} \xrightarrow{k_d} TES_{surf.}$$ (Eq. S22a)

$$Au_{ads.}^{III} + TES_{surf.} \xrightarrow{k_2'} Au_{ads.}^{I}$$ (Eq. S22b)

For the same reasons as those given above, the consumption rate of Au^{III} ions is expressed by :

$$\frac{d[Au^0]}{dt} = -\frac{d[Au_{tot.}^{III}]}{dt} = k_2'[Au_{ads.}^{III}][TES_{surf.}]$$ (Eq. S35)

According to Eq. S22a,b the consumption rate of TES at the particle surface is given by :

$$-\frac{d[TES_{surf.}]}{dt} = k_2'[Au_{ads.}^{III}][TES_{surf.}] - k_d[TES_{sol.}]$$ (Eq. S36)

Let us consider now that the diffusion of the TES from the solution to the primary particle surface is the limiting step. In steady state : $-\frac{d[TES_{surf.}]}{dt} = 0$

and

$$-\frac{d[Au_{tot.}^{III}]}{dt} = k_d[TES_{sol.}]$$ (Eq. S37)

In case of diffusion-limited step, the surface reaction is much faster than the diffusion, a considering spherical nanoparticles, the constant k_d takes the expression:

$$k_d = N_p 4\pi D \frac{Rr}{R-r}$$ (Eq. S38)

with N_p the concentration of particle, D the diffusion coefficient of TES, r the nanoparticle radius and R the capture radius (R >>r in the diluted regime).

For $N_p = ND = 4\times10^{16}$ cm^{-3} the capture radius is found equal to $R = \sqrt[3]{\frac{3}{4\pi \times ND}} \approx 18\ nm$

For r = 0.8 nm and with D in the range 1×10^{-9} - 4×10^{-9} m^2.s^{-1}, the constant rate k_d is found in the range : 4×10^5 s^{-1} - 16×10^5 s^{-1}

These values are several orders of magnitude higher than the experimental value.

Thus, a growth regime limited by the diffusion of TES is not realistic unless TES diffusion is significantly reduced in the reaction medium. One alternative would be that the diffusion of TES through the ligand layer capping the particles is strongly hindered with a diffusion coefficient several order of magnitude lower than in pure hexane.

IX. References of supplementary information

1 P. Juhás, T. Davis, C. L. Farrow and S. J. L. Billinge, *J. Appl. Crystallogr.*, 2013, **46**, 560–566.

2 A. Hjorth Larsen, J. Jørgen Mortensen, J. Blomqvist, I. E. Castelli, R. Christensen, M. Dułak, J. Friis, M. N. Groves, B. Hammer, C. Hargus, E. D. Hermes, P. C. Jennings, P. Bjerre Jensen, J. Kermode, J. R. Kitchin, E. L. Kolsbjerg, J. Kubal, K. Kaasbjerg, S. Lysgaard, J. B. Maronsson, T. Maxson, T. Olsen, L. Pastewka, A. Peterson, C. Rostgaard, J. Schiøtz, O. Schütt, M. Strange, K. S. Thygesen, T. Vegge, L. Vilhelmsen, M. Walter, Z. Zeng, K. W. Jacobsen, *J. Phys. Condens. Matter*, 2017, **29**, 273002.

3 R. K. Ramamoorthy, E. Yildirim, I. Rodriguez-Ruiz, P. Roblin, L.-M. Lacroix, A. Diaz, R. Parmar, S. Teychené and G. Viau, *Lab. Chip* 2024, **24**, 327–338.

4 R. K. Ramamoorthy, E. Yildirim, E. Barba, P. Roblin, J. A. Vargas, L.-M. Lacroix, I. Rodriguez-Ruiz, P. Decorse, V. Petkov, S. Teychené and G. Viau, *Nanoscale*, 2020, **12**, 16173-16188.

5 B. Hammouda, *J. Appl. Cryst.*, 2010, **43**, 716–719.

6 https://sasview.github.io/ (accessed 2024-08-23).

7 https://www.sasview.org/docs/user/models/guinier_porod.html

8 F. Neese, *WIREs Comput Mol Sci.*, 2022, **12**, e1606.

9 C. Adamo and V. Barone, *J. Chem. Phys.*, 1999, **110**, 6158–6170.

10 E. Caldeweyher, S. Ehlert, A. Hansen, H. Neugebauer, S. Spicher, C. Bannwarth and S. Grimme, *J. Chem. Phys.*, 2019, **150**, 154122.

11 F. Weigend and R. Ahlrichs, *Phys. Chem. Chem. Phys.*, 2005, **7**, 3297–3305.

12 F. Neese, F. Wennmohs, A. Hansen and U. Becker, *Chem. Phys.,* 2009, **356**, 98–109.

13 J. Tomasi, B. Mennucci and R. Cammi, *Chem. Rev.*, **2005**, *105*, 2999–3094.

14 C. Bannwarth, E. Caldeweyher, S. Ehlert, A. Hansen, P. Pracht, J. Seibert, S. Spicher and S. Grimme, *WIREs Comput. Mol. Sci.*, 2020, **11**, e01493.

15 C. Bannwarth, S. Ehlert and S. Grimme, *J. Chem. Theory Comput.*, 2019, **15**, 1652-1671.

16 S. Ehlert, M. Stahn, S. Spicher and S. Grimme, *J. Chem. Theory Comput.*, 2021, **17**, 4250-4261.

17 W. Humphrey, A. Dalke and K. Schulten, *J. Mol. Graph.* 1996, **14**, 33–38.

18 National Center for Biotechnology Information. PubChem Compound Summary for CID 5356789, Oleylamine https://pubchem.ncbi.nlm.nih.gov/compound/Oleylamine and CID 21863413, Hydrogen Tetrachloroaurate(III) Trihydrate https://pubchem.ncbi.nlm.nih.gov/compound/Hydrogen-Tetrachloroaurate_III_-Trihydrate.

19 E. F. Pettersen, T. D. Goddard, C. C. Huang, G. S. Couch, D. M. Greenblatt, E. C. Meng and T. E. Ferrin, *J. Comput. Chem.* 2004, **25**, 1605-12.

20 L. Martínez, R. Andrade, E. G. Birgin and J. M. Martínez, *J. Comput. Chem*., 2009, **30**, 2157-2164.

21 https://www.sasview.org/ docs/user/models/sphere.html

22 A. Loubat, L.-M. Lacroix, A. Robert, M. Impéror-Clerc, R. Poteau, L. Maron, R. Arenal, B. Pansu and G. Viau, *J. Phys. Chem. C*, 2015, **119**, 4422–4430.

23 E. Yildirim, R. K. Ramamoorthy, R. Parmar, P. Roblin, J. A. Vargas, V. Petkov, A. Diaz, S. Checchia, I. Rodriguez Ruiz, S. Teychené, L.-M. Lacroix and G. Viau, *J. Phys. Chem. C*, 2023, **127**, 3047–3058.